

KXNet: A Model-Driven Deep Neural Network for Blind Super-Resolution

Jiahong Fu¹, Hong Wang², Qi Xie^{*1}, Qian Zhao¹, Deyu Meng^{1,3}, and Zongben Xu^{1,3}

¹ Xi'an Jiaotong University, Shaanxi, P.R. China
jiahongfu@stu.xjtu.edu.cn, {xie.qi, timmy.zhaoqian, dymeng, zbxu}@mail.xjtu.edu.cn

² Tencent Jarvis Lab, Shenzhen, P.R. China
hazelhwang@tencent.com

³ Pazhou Lab, Guangzhou, P.R. China

Abstract. Although current deep learning-based methods have gained promising performance in the blind single image super-resolution (SISR) task, most of them mainly focus on heuristically constructing diverse network architectures and put less emphasis on the explicit embedding of the physical generation mechanism between blur kernels and high-resolution (HR) images. To alleviate this issue, we propose a model-driven deep neural network, called KXNet, for blind SISR. Specifically, to solve the classical SISR model, we propose a simple-yet-effective iterative algorithm. Then by unfolding the involved iterative steps into the corresponding network module, we naturally construct the KXNet. The main specificity of the proposed KXNet is that the entire learning process is fully and explicitly integrated with the inherent physical mechanism underlying this SISR task. Thus, the learned blur kernel has clear physical patterns and the mutually iterative process between blur kernel and HR image can soundly guide the KXNet to be evolved in the right direction. Extensive experiments on synthetic and real data finely demonstrate the superior accuracy and generality of our method beyond the current representative state-of-the-art blind SISR methods. Code is available at: <https://github.com/jiahong-fu/KXNet>.

Keywords: Blind Single Image Super-Resolution, Physical Generation Mechanism, Model-Driven, Kernel Estimation, Mutual Learning

1 Introduction

Single image super-resolution (SISR) has been widely adopted in various vision applications, *e.g.* video surveillance, medical imaging, and video enhancement. For this SISR task, the main goal is to reconstruct the high-resolution (HR) image with high visual quality from an observed low-resolution (LR) image.

* Corresponding author.

Specifically, in traditional SISR framework, the degradation process for an LR image \mathbf{Y} can be mathematically expressed as [11,12]:

$$\mathbf{Y} = (\mathbf{X} \otimes \mathbf{K}) \downarrow_s + \mathbf{N}, \quad (1)$$

where \mathbf{X} is the to-be-estimated HR image; \mathbf{K} is a blur kernel; \otimes denotes two-dimensional (2D) convolution operation; \downarrow_s represents the standard s -fold downsampler, *i.e.*, only keeping the upper-left pixel for each distinct $s \times s$ patch [53]; \mathbf{N} denotes the Additive White Gaussian Noise (AWGN) with noise level σ . Clearly, estimating \mathbf{X} and \mathbf{K} from \mathbf{Y} is an ill-posed inversion problem.

With the rapid development of deep neural networks (DNNs), in recent years, many deep learning (DL)-methods have been proposed for this SISR task [19,21,24,60,59,31,22]. Albeit achieving promising performance in some scenes, the assumption that the blur kernel \mathbf{K} is known, such as bicubic [7,19,24,59,60], would make these methods tend to fail in real applications where the practical degradation process is always complicated. To alleviate this issue, researchers have focused on the more challenging blind super-resolution (SR) task where the blur kernel \mathbf{K} is unknown. Currently, blind SR methods can be mainly divided into two categories: traditional-model-based ones and DL-based ones.

Specifically, conventional blind SR works [27,6] aim to formulate the hand-crafted prior knowledge of blur kernel \mathbf{K} and HR image \mathbf{X} , into an optimization algorithm to constrain the solution space of the ill-posed SISR problem. Due to the involved iterative computations, these methods are generally time-consuming. Besides, the manually-designed priors cannot always sufficiently represent the complicated and diverse images in real scenarios.

Recently, to flexibly deal with multi-degradation situations, some DL-based blind SR methods [58,3,23] have been proposed, which are composed of two successive steps, *i.e.*, blur kernel estimation and non-blind super-resolver. Since these two steps are independently handled, the estimated blur kernel and the recovered HR image are possibly not compatible well. To further boost the performance, some works [14,25,43,54,44] directly utilized off-the-shelf network modules to recover HR images in an end-to-end manner without fully embedding the physical generation mechanism underlying this SISR task.

Very recently, the end-to-end deep unfolding framework has achieved good performance in this SISR task [16,5,53,25]. Typically, by alternately updating the blur kernel \mathbf{K} and the HR image \mathbf{X} , the blind SR work [25] heuristically constructs an optimization-inspired SR network. However, there are two main limitations: 1) the inherent physical generation mechanism in Eq. (1) is still not fully and explicitly embedded into the iterative computations of \mathbf{K} and \mathbf{X} , and every network module has relatively weak physical meanings; 2) most of these deep unfolding-based methods cannot finely extract blur kernels with clear physical patterns, which is caused by weak interpretable operations on blur kernels, such as concatenation and stretching [25] and spatial feature transform (SFT) layer [14]. Hence, there is still room for further performance improvement.

To alleviate these issues, we propose a novel deep unfolding blind SR network that explicitly embeds the physical mechanism in Eq. (1) into the mutual learning

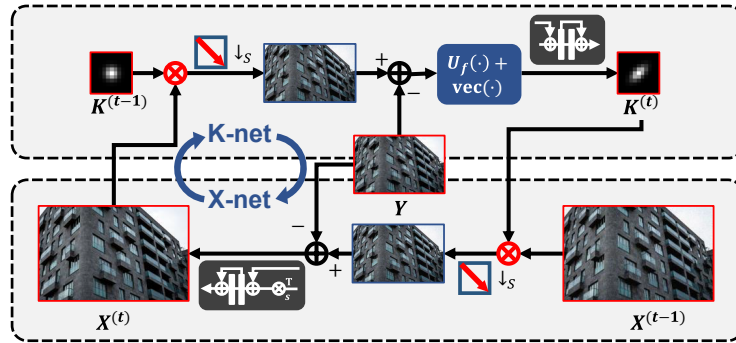


Fig. 1: Illustration of the proposed KXnet where K-net for blur kernel estimation and X-net for HR image estimation are constructed based on the physical generation mechanism in Eq. (1).

between blur kernel and HR image in a sufficient manner. Under the explicit guidance of the degradation process Eq. (1), the updating of \mathbf{K} and \mathbf{X} finely proceeds, and the learned blur kernel presents clear structural patterns with specific physical meanings. In summary, our contributions are mainly three-fold:

- We propose a novel model-driven deep unfolding blind super-resolution network (called KXNet) to jointly estimate the blur kernel \mathbf{K} and the HR image \mathbf{X} , which is explicitly integrated with the physical generation mechanism in Eq. (1), as shown in Fig. 1. Specifically, we propose an iterative algorithm to solve the classical degradation model Eq. (1) and then construct the KXNet by unfolding the iterative steps into the corresponding network modules. Naturally, the mutually iterative learning process between blur kernel and HR image fully complies with the inherent physical generation mechanism, and every network module in KXNet has clear physical interpretability.
- Instead of heuristic operations (*e.g.* concatenation and affine transformation) on blur kernel in most of the current SR methods, the learning and estimation of blur kernel in our method is proceeding under the guidance of Eq. (1) and thus has clearer physical meanings. As shown in Fig. 1, the K-net is finely corresponding to the iterative steps for updating blur kernel and thus the extracted blur kernel \mathbf{K} has reasonable and clear physical structures. Besides, attributed to the intrinsic embedding of the physical generation mechanism, we maintain the essential convolution computation between blur kernel and HR image, which is expected to achieve better SR performance.
- Extensive experiments executed on synthetic and real data comprehensively demonstrate the superiority of the proposed KXNet in SR performance and model generalizability beyond the current state-of-the-art (SOTA) methods. Besides, more analysis and network visualization validate the rationality and effectiveness of our method, and the extracted blur kernels with clear structures would be helpful for other vision tasks in real applications.

2 Related Work

2.1 Non-Blind Single Image Super-Resolution

In recent years, deep learning (DL) has achieved great progress in SISR task. Current SISR methods mainly focus on utilizing deep neural networks to learn the mapping function from a low-resolution (LR) image to the corresponding high-resolution (HR) image via paired training data. Since it is very time-consuming and labor-intensive to pre-collect massive paired LR-HR images, many researchers adopt the manually-designed degradation processes to generate the LR images, such as the classical bicubic interpolation (\mathbf{K} in Eq. (1) is set as the bicubic kernel). This setting has been widely adopted from the early SRCNN [7] to the recent various SISR methods [24,59,31,22]. These methods aim to design diverse network modules to improve the SISR performance.

Considering that in real scenes, the degradation process is always complicated, there are some works [57,48,53] dealing with multiple degradation forms. For example, SRMD [57] takes different degradation feature maps as additional inputs for the SR task. Very recently, Zhang [53] constructs an optimization-inspired non-blind SISR network for handling the multiple degradation scenes.

2.2 Blind Single Image Super-Resolution

To better represent the real degradation process and improve the SR performance in real-world, blind single image super-resolution has been attracting the attention of researchers in this field. In this case, the goal is to jointly estimate the unknown blur kernel \mathbf{K} and the expected HR image \mathbf{X} . Currently, against this task, the existing methods can be mainly categorized into two groups: two-step methods and end-to-end methods.

Two-step Blind Super-Resolution. In this research line, researchers first estimate the blur kernel based on different prior knowledge [32,49,34,23]. For example, Michaeli [30] utilizes the inter-scale recurrence property of an image to help extract the blur kernel. Then by inserting the estimated blur kernel into non-blind SR methods[58], the corresponding SR results can be restored. Recently, Kligler [3] have proposed an unsupervised KernelGAN to estimate the blur kernel based on the recurrence property of the image patch, then utilized the extracted kernel to help reconstruct SR images. Similarly, Liang [23] have proposed a flow-based architecture to capture the prior knowledge of the blur kernel which can be used for the subsequent non-blind SR task. Most of these two-step methods have not fully considered the iterative and mutual learning between blur kernels and HR images.

End-to-End Blind Super-Resolution. Very recently, some works begin to emphasize how to merge the kernel estimation process with the non-blind SR process and thus design an end-to-end blind SR framework. Gu [14] firstly designed a single network architecture that contains a kernel estimation module and a non-blind SR module. However, this method needs to separately train

multiple modules. To alleviate this issue, Luo [25,26] proposed a complete end-to-end network that can be trained in an end-to-end manner. Wang [43] proposed an unsupervised degradation representation learning scheme and then utilized it to help accomplish the blind SR task. Zhang [54] and Wang [44] design a “high-order” degradation model to simulate the image degradation process.

Albeit achieving promising performance in some scenarios, most of these methods have the following limitations: 1) The estimated degradation form has relatively weak physical meanings or cannot fully reflect blur kernels with clear and structural patterns; 2) The degradation representation is heuristically used, such as simple concatenation with LR image, without explicitly reflecting the inherent convolution operation between blur kernel and image; 3) The intrinsic physical generation mechanism in Eq. (1) has not been fully embedded into network design. To alleviate these issues, we adopt the deep unfolding technique [46,42], with several novel designs, for better embedding the inherent mechanism into network structure and improving the performance in blind SR restoration.

3 Blind Single Image Super-Resolution Model

In this section, for the blind SISR task, we formulate the corresponding mathematical model and propose an optimization algorithm.

3.1 Model Formulation

From Eq. (1), given an observed LR image $\mathbf{Y} \in \mathbb{R}^{h \times w}$, our goal is to estimate the two unknown variables, *i.e.*, blur kernel $\mathbf{K} \in \mathbb{R}^{p \times p}$ and HR image $\mathbf{X} \in \mathbb{R}^{H \times W}$. Correspondingly, we can formulate the following optimization problem as:

$$\begin{aligned} \min_{\mathbf{K}, \mathbf{X}} & \left\| \mathbf{Y} - (\mathbf{X} \otimes \mathbf{K}) \downarrow_s \right\|_F^2 + \lambda_1 \phi_1(\mathbf{K}) + \lambda_2 \phi_2(\mathbf{X}) \\ \text{s.t. } & \mathbf{K}_j \geq 0, \sum_j \mathbf{K}_j = 1, \forall j, \end{aligned} \quad (2)$$

where $\phi_1(\mathbf{K})$ and $\phi_2(\mathbf{X})$ represent the regularizers for delivering the prior knowledge of blur kernel and HR image, respectively; λ_1 and λ_2 are trade-off regularization parameters. Similar to [33,37,34], we introduce the non-negative and equality constraints for every element \mathbf{K}_j in blur kernel \mathbf{K} . Specifically, the data fidelity term (*i.e.*, the first term in the objective function of Eq. (2)) represents the physical generation mechanism, which would provide the explicit guidance during the iterative updating of \mathbf{K} and \mathbf{X} , and the prior terms $\phi_1(\mathbf{K})$ and $\phi_2(\mathbf{X})$ enforce the expected structures of the solution for this ill-posed problem.

Instead of adopting hand-crafted prior functions as in conventional optimization-based SR methods, we utilize a data-driven strategy to flexibly extract the implicit prior knowledge underlying \mathbf{X} and \mathbf{K} from data via DNNs in an end-to-end manner. This operation has been fully validated to be effective in many diverse vision tasks by extensive studies [55,46,42]. The details for learning $\phi_1(\mathbf{K})$ and $\phi_2(\mathbf{X})$ are given in Sec. 4.

3.2 Model Optimization

For this blind SISR task, our goal is to build a deep unfolding network where network modules are possibly corresponding to iterative steps involved in an optimization algorithm so as to make the network interpretable and easily controllable. Thus, it is necessary to derive an iterative algorithm for solving the SR problem in Eq. (2). To this end, we adopt a proximal gradient technique [2,13] to alternatively update the blur kernel \mathbf{K} and HR image \mathbf{X} . Then, the derived optimization algorithm contains only simple operators which makes it possible to be easily unfolded into network modules, as shown in following.

Updating blur kernel \mathbf{K} : The blur kernel \mathbf{K} can be optimized by solving the quadratic approximation [2] of the problem Eq. (2) with respect to the variable \mathbf{K} , expressed as:

$$\begin{aligned} \min_{\mathbf{K}} & \left\| \mathbf{K} - \left(\mathbf{K}^{(t-1)} - \delta_1 \nabla f \left(\mathbf{K}^{(t-1)} \right) \right) \right\|_F^2 + \lambda_1 \delta_1 \phi_1(\mathbf{K}) \\ \text{s.t.} & \mathbf{K}_j \geq 0, \sum_j \mathbf{K}_j = 1, \forall j, \end{aligned} \quad (3)$$

where $\mathbf{K}^{(t-1)}$ denotes the updating result after the last iteration; δ_1 denotes the stepsize parameter; $f(\mathbf{K}^{(t-1)}) = \left\| \mathbf{Y} - \left(\mathbf{X}^{(t-1)} \otimes \mathbf{K}^{(t-1)} \right) \downarrow_{\mathbf{s}} \right\|_F^2$. For a general regularizer $\phi_1(\cdot)$, the solution of Eq. (3) can be easily expressed as [8]:

$$\mathbf{K}^{(t)} = \text{prox}_{\lambda_1 \delta_1} \left(\mathbf{K}^{(t-1)} - \delta_1 \nabla f \left(\mathbf{K}^{(t-1)} \right) \right), \quad (4)$$

where the specific form of $\nabla f(\mathbf{K}^{(t-1)})$ is complicated. For ease of calculation, by transforming the convolutional operation in $f(\mathbf{K}^{(t-1)})$ into matrix multiplication, we can derive that:

$$\begin{aligned} f(\mathbf{k}^{(t-1)}) &= \text{vec} \left(\left\| \mathbf{Y} - \left(\mathbf{X}^{(t-1)} \otimes \mathbf{K}^{(t-1)} \right) \downarrow_{\mathbf{s}} \right\|_F^2 \right) \\ &= \left\| \mathbf{y} - D_{\mathbf{s}} U_f \left(\mathbf{X}^{(t-1)} \right) \mathbf{k}^{(t-1)} \right\|_F^2, \end{aligned} \quad (5)$$

where $\mathbf{y} = \text{vec}(\mathbf{Y})$ and $\mathbf{k} = \text{vec}(\mathbf{K})$ denote the vectorizations of \mathbf{Y} and \mathbf{K} , respectively; $\mathbf{y} \in \mathbb{R}^{hw \times 1}$; $\mathbf{k} \in \mathbb{R}^{p^2 \times 1}$; $U_f(\mathbf{X}^{(t-1)}) \in \mathbb{R}^{HW \times p^2}$ are the unfolded result of $\mathbf{X}^{(t-1)}$ (see Fig. 2); $D_{\mathbf{s}}$ denotes the downsampling operator which is corresponding to the operator $\downarrow_{\mathbf{s}}$, and achieves the transformation from the size HW to the size hw . Thus, the result $D_{\mathbf{s}} U_f(\mathbf{X}^{(t-1)})$ ⁴ has the size with $hw \times p^2$

⁴ More derivations are provided in the supplementary material.

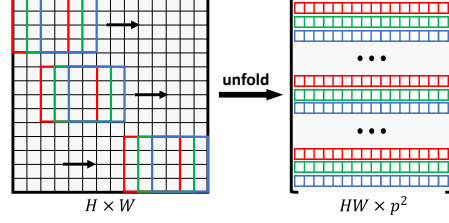


Fig. 2: Illustration of the operator $U_f(\cdot)$.

and $\nabla f(\mathbf{k}^{(t-1)})$ is derived as:

$$\nabla f(\mathbf{k}^{(t-1)}) = \left(D_s U_f(\mathbf{X}^{(t-1)}) \right)^T \text{vec} \left(\mathbf{Y} - \left(\mathbf{X}^{(t-1)} \otimes \mathbf{K}^{(t-1)} \right) \downarrow_s \right), \quad (6)$$

where $\nabla f(\mathbf{k}^{(t-1)}) \in \mathbb{R}^{p^2 \times 1}$; $\nabla f(\mathbf{K}^{(t-1)}) = \text{vec}^{-1}(\nabla f(\mathbf{k}^{(t-1)}))$; $\text{vec}^{-1}(\cdot)$ is the reverse vectorization; $\text{prox}_{\lambda_1 \delta_1}(\cdot)$ is the proximal operator dependent on the regularization term $\phi_1(\cdot)$ with respect to \mathbf{K} . Different from the traditional methods with hand-crafted regularization terms, we rely on the powerful fitting capability of residual networks to automatically learn the implicit proximal operator $\text{prox}_{\lambda_1 \delta_1}(\cdot)$ via training data. Such operations have achieved great success in other deep unfolding works [46,42]. The details are described in Sec. 4.

Updating HR image \mathbf{X} : Similarly, the quadratic approximation of the problem in Eq. (2) with respect to \mathbf{X} can be derived as:

$$\min_{\mathbf{X}} \left\| \mathbf{X} - \left(\mathbf{X}^{(t-1)} - \delta_2 \nabla h(\mathbf{X}^{(t-1)}) \right) \right\|_F^2 + \lambda_2 \delta_2 \phi_2(\mathbf{X}), \quad (7)$$

where $h(\mathbf{X}^{(t-1)}) = \left\| \mathbf{Y} - \left(\mathbf{X}^{(t-1)} \otimes \mathbf{K}^{(t)} \right) \downarrow_s \right\|_F^2$; With $\nabla h(\mathbf{X}^{(t-1)}) = \mathbf{K}^{(t)} \otimes_s^T \left(\mathbf{Y} - \left(\mathbf{X}^{(t-1)} \otimes \mathbf{K}^{(t)} \right) \downarrow_s \right)$, we can deduce the updating rule for \mathbf{X} as:

$$\mathbf{X}^{(t)} = \text{prox}_{\lambda_2 \delta_2} \left(\mathbf{X}^{(t-1)} - \delta_2 \mathbf{K}^{(t)} \otimes_s^T \left(\mathbf{Y} - \left(\mathbf{X}^{(t-1)} \otimes \mathbf{K}^{(t)} \right) \downarrow_s \right) \right), \quad (8)$$

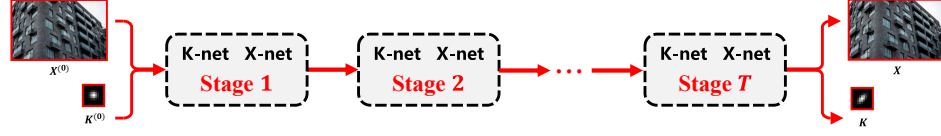
where $\text{prox}_{\lambda_2 \delta_2}(\cdot)$ is the proximal operator dependent on the regularization term $\phi_2(\cdot)$ about \mathbf{X} ; \otimes_s^T denotes the transposed convolution operation with stride as s . Similar to $\text{prox}_{\lambda_1 \delta_1}(\cdot)$, we adopt deep network to flexibly learn the $\text{prox}_{\lambda_2 \delta_2}(\cdot)$.

As seen, the proposed optimization algorithm is composed of the iterative rules Eq. (4) and Eq. (8). By unfolding every iterative step into the corresponding network module, we can naturally build the deep unfolding network architecture for solving the blind SISR task as given in Eq. (2).

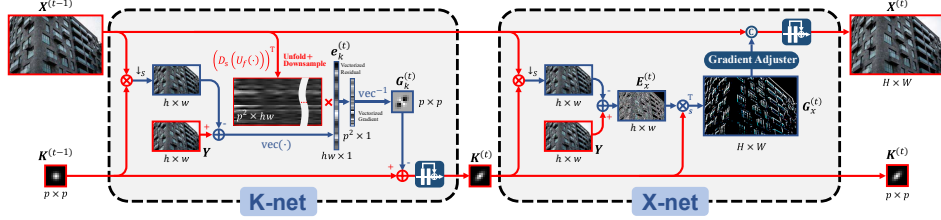
4 Blind Super-Resolution Unfolding Network

Recently, deep unfolding techniques have achieved great progress in various computer vision fields [51,50,39,40,41], such as spectral image fusion [46,47], de-raining [42], and non-blind super-resolution [53]. Inspired by these methods, in this section, we aim to build an end-to-end deep unfolding network for blind super-resolution problem by unfolding each iterative step involved in Eq. (4) and Eq. (8) as the corresponding network module.

As shown in Fig. 3(a), the proposed network consists of T stages, which correspond to T iterations of the proposed optimization algorithm for solving the problem in Eq. (2). At each stage, as illustrated in Fig. 3(b), the network is subsequently composed of K-net and X-net. In specific, the K-net takes the LR image \mathbf{Y} , the estimated blur kernel $\mathbf{K}^{(t-1)}$ and the estimated HR image $\mathbf{X}^{(t-1)}$ as inputs and outputs the updated $\mathbf{K}^{(t)}$. Then, X-net takes \mathbf{Y} , $\mathbf{K}^{(t)}$, and $\mathbf{X}^{(t-1)}$ as inputs, and outputs the updated $\mathbf{X}^{(t)}$. This alternative iterative process complies with the proposed algorithm.



(a) The algorithm processes of the entire KXNet.



vec(\cdot): vectorization $U_f(\cdot)$: unfolding D_s : downsampling $(\cdot)^T$: matrix transposing \boxplus : proxNet \oplus : concat

(b) The network architecture of K-net and X-net at each stage.

Fig. 3: (a) The overall architecture of the proposed KXNet contains T stages. It inputs the initialized HR image $\mathbf{X}^{(0)}$ and initialized blur kernel $\mathbf{K}^{(0)}$, and outputs the HR image \mathbf{X} and the blur kernel \mathbf{K} . (b) The network architecture at the t^{th} stage, which consists of K-net and X-net for updating the blur kernel \mathbf{K} and HR image \mathbf{X} , respectively.

4.1 Network Module Design

By step-by-step decomposing the iterative rules of Eq. (4) and Eq. (8) into sub-steps and then unfolding them as the fundamental network modules, we can easily construct the entire deep unfolding framework. However, the key problem is how to deal with the implicit proximal operators $\text{prox}_{\lambda_1 \delta_1}(\cdot)$ and $\text{prox}_{\lambda_2 \delta_2}(\cdot)$. As stated in Sec. 3.2, following the current other unfolding-based networks [46, 42], we can utilize ResNet [15] to construct $\text{prox}_{\lambda_1 \delta_1}(\cdot)$ and $\text{prox}_{\lambda_2 \delta_2}(\cdot)$. Thus, at the t^{th} stage, the network is built as:

$$\text{K-net: } \begin{cases} \mathbf{e}_k^{(t)} = \text{vec} \left(\mathbf{Y} - \left(\mathbf{X}^{(t-1)} \otimes \mathbf{K}^{(t-1)} \right) \downarrow_s \right) \\ \mathbf{G}_k^{(t)} = \text{vec}^{-1} \left(\left(D_s U_f \left(\mathbf{X}^{(t-1)} \right) \right)^T \mathbf{e}_k^{(t)} \right) \\ \mathbf{K}^{(t)} = \text{proxNet}_{\theta_k^{(t)}} \left(\mathbf{K}^{(t-1)} - \delta_1 \left(\mathbf{G}_k^{(t)} \right) \right), \end{cases} \quad (9)$$

$$\text{X-net: } \begin{cases} \mathbf{E}_x^{(t)} = \mathbf{Y} - \left(\mathbf{X}^{(t-1)} \otimes \mathbf{K}^{(t)} \right) \downarrow_s \\ \mathbf{G}_x^{(t)} = \mathbf{K}^{(t)} \otimes_s^T \mathbf{E}_x^{(t)} \\ \hat{\mathbf{G}}_x^{(t)} = \text{adjuster} \left(\mathbf{G}_x^{(t)} \right) \\ \mathbf{X}^{(t)} = \text{proxNet}_{\theta_x^{(t)}} \left(\mathbf{X}^{(t-1)}, \hat{\mathbf{G}}_x^{(t)} \right), \end{cases} \quad (10)$$

where $\text{proxNet}_{\theta_k^{(t)}}$ and $\text{proxNet}_{\theta_x^{(t)}}$ are two shallow ResNets with the parameters $\theta_k^{(t)}$ and $\theta_x^{(t)}$ at the t -th stage, respectively; $\text{adjuster}(\cdot)$ is an operation for boosting the gradient, whose details are discussed later. All these network parameters

can be automatically learned from training data in an end-to-end manner. Note that the proximal gradient descent algorithm usually needs lots of iterations for convergence, which will lead to too many network stages when adopting the unfolding technique. To avoid this issue, as shown in the last equation of Eq. (10), instead of directly adopting the subtraction between $\mathbf{X}^{(t-1)}$ and $\hat{\mathbf{G}}_x^{(t)}$, we concatenate $\mathbf{X}^{(t-1)}$ and $\hat{\mathbf{G}}_x^{(t)}$ as the input of the proximal network $\text{proxNet}_{\theta_x^{(t)}}(\cdot)$, which introduces more flexibility to the combination of $\mathbf{X}^{(t-1)}$ and $\hat{\mathbf{G}}_x^{(t)}$.

Remark for K-net. The proposed KXNet has clear physical interpretability. Different from the current most deep blind SR methods which heuristically adopt the concatenation or affine transformation operators on $\mathbf{K}^{(t-1)}$ to help the learning of HR images, the proposed K-net is constructed based on the iterative rule in Eq. (4) and every network sub-module has its specific physical meanings as shown in Fig. 3(b). Specifically, following the degradation model, $\mathbf{X}^{(t-1)}$ is convolved with $\mathbf{K}^{(t-1)}$ followed by the downsampling operator. Then by subtracting the result from \mathbf{Y} , we get the residual information $\mathbf{e}_k^{(t)}$, which is actually the key information for updating the current estimation. Then, we regard $\mathbf{e}_k^{(t)}$ as a weight and adopt it to perform a weighted summation on the corresponded patches in $\mathbf{X}^{(t-1)}$ (i.e., row vectors in $D_s U_f(\mathbf{X}^{(t-1)}) \in \mathbb{R}^{hw \times p^2}$, as shown in Fig. 3(b)), and get $\mathbf{G}_k^{(t)}$ for updating $\mathbf{K}^{(t-1)}$. Actually, this is consistent with the relationship between $\mathbf{K}^{(t-1)}$ and $\mathbf{X}^{(t-1)}$, since convolution operation is executed based on the patch with $p \times p$.

Gradient adjuster. For X-net, an adjuster is adopted to the gradient $\mathbf{G}_x^{(t)}$ as shown in the third equation of Eq. (10). Specifically, the transposed convolution $\mathbf{G}_x^{(t)}$ in X-net can easily cause “uneven overlap”, putting more of the metaphorical paint in some places than others [9,36], which is unfriendly to the reconstruction of HR images. To alleviate the unevenness issue, we introduce the operator $\mathbf{K}^{(t)} \otimes_s^T \mathbf{1}$ and the adjusted gradient $\hat{\mathbf{G}}_x^{(t)}$ is⁵:

$$\hat{\mathbf{G}}_x^{(t)} = \frac{\mathbf{G}_x^{(t)}}{\mathbf{K}^{(t)} \otimes_s^T \mathbf{1}}, \quad (11)$$

where $\mathbf{1} \in \mathbb{R}^{h \times w}$ is a matrix with all elements as 1.

4.2 Network Training

To train the proposed deep unfolding blind SR network, we utilize the L_1 loss [61] to supervise the predicted blur kernel $\mathbf{K}^{(t)}$ and the estimated HR image $\mathbf{X}^{(t)}$ at each stage. Correspondingly, the total objective function is:

$$L = \sum_{t=1}^T \alpha_t \|\mathbf{K} - \mathbf{K}^{(t)}\|_1 + \sum_{t=1}^T \beta_t \|\mathbf{X} - \mathbf{X}^{(t)}\|_1, \quad (12)$$

where $\mathbf{K}^{(t)}$ and $\mathbf{X}^{(t)}$ are obtained based on the updating process in Eq. (9) and Eq. (10) at the t^{th} stage, respectively; α_t and β_t are trade-off parameters⁶. $\mathbf{X}^{(0)}$ is initialized as the bicubic upsampling of the LR image \mathbf{Y} , and $\mathbf{K}^{(0)}$ is initialized as a standard Gaussian kernel.

⁵ More analysis is provided in the supplementary material.

⁶ We set $\alpha_t = \beta_t = 0.1$ at middle stages, $\alpha_T = \beta_T = 1$ at the last stage, and $T = 19$.

5 Experimental Results

5.1 Details Descriptions

Synthesized Datasets. Following [14,25,43], we collect 800 HR images from DIV2K [1] and 2650 HR images from Flickr2K [38] to synthesize the training data, and adopt the four commonly-used benchmark datasets, *i.e.*, Set5 [4], Set14 [52], BSD100 [28], and Urban100 [17], to synthesize the testing data. During the synthesis process of training and testing pairs, we adopt the degradation process in Eq. (1) with two different degradation settings: 1) isotropic Gaussian blur kernel with noise free; 2) anisotropic Gaussian blur kernel with noise [10,35,53,23], and set the s -fold downsampler as in [3,53,23]. Note that as stated in [35,53], the later setting is very close to the real SISR scenario.

In setting 1), for training set, following [14,25,43], the blur kernel size $p \times p$ is set as 21×21 for all scales $\mathbf{s} \in \{2, 3, 4\}$ and the corresponding kernel width for different scales ($\times 2$, $\times 3$, and $\times 4$ SR) is uniformly sampled from the ranges $[0.2, 2.0]$, $[0.2, 3.0]$, and $[0.2, 4.0]$, respectively. For testing set, the blur kernel is set as *Gaussian8* [14], which uniformly samples 8 kernels from the ranges $[0.8, 1.6]$, $[1.35, 2.40]$, and $[1.8, 3.2]$ for the scale factors 2, 3, and 4, respectively.

In setting 2), for trainings set, we set the kernel size p as 11/15/21 for $\times 2/3/4$ SR, respectively. Specifically, the kernel width at each axis are obtained by randomly rotating the widths λ_1 and λ_2 with an angle $\theta \sim U[-\pi, \pi]$, where λ_1 and λ_2 are uniformly distributed in $U(0.6, 5.0)$. Besides, the range of noise level σ is set to $[0, 25]$. For testing set, we separately set the kernel width as $\lambda_1 = 0.8, \lambda_2 = 1.6$ and $\lambda_1 = 2.0, \lambda_2 = 4.0$, and rotate them by $\theta \in \{0, \frac{\pi}{4}, \frac{\pi}{2}, \frac{3\pi}{4}\}$, respectively. This means every HR testing image is degraded by 8 different blur kernels.

Real Dataset. To verify the performance of the proposed method in real scenarios, we use the dataset RealSRSet [54] for generalization evaluation, which includes 20 real LR images collected from various sources [18,28,29,56].

Training Details. Based on the PyTorch framework executed on two RTX2080Ti GPUs, we adopt the Adam solver [20] with the parameters as $\beta_1 = 0.9$ and $\beta_2 = 0.99$ to optimize the proposed network with the batch size and patch size set as 12 and 64×64 , respectively. The learning rate is initialized as 2×10^{-4} and decays by multiplying a factor of 0.5 at every 2×10^5 iteration. The training process ends when the learning rate decreases to 1.25×10^{-5} .

Comparison Methods. We comprehensively substantiate the superiority of our method by comparing it with several recent SOTA methods, including the non-blind SISR method RCAN [59], and blind SISR methods, including IKC [14], DASR [43], and DAN [25]. For a fair comparison, we have retrained IKC, DASR, and DAN based on the aforementioned two settings with the public codes.

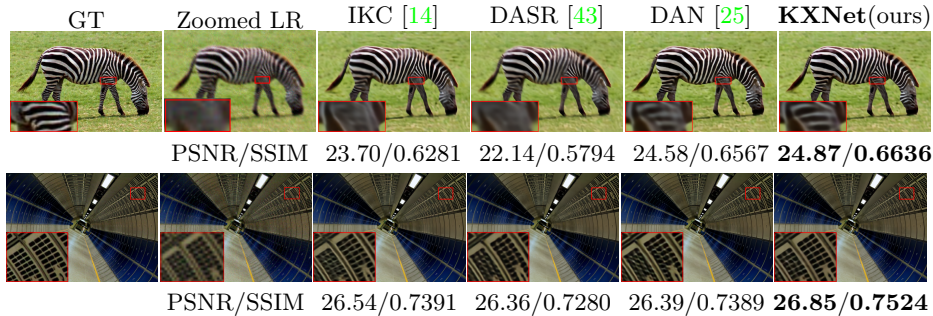
Performance Evaluation. For synthetic data, we adopt the PSNR and SSIM [45] computed on Y channel in YCbCr space. While for RealSRSet, we only provide the visual results since there is no ground-truth (GT) image.

5.2 Experiments on Synthetic Data

Tab. 1 reports the average PSNR and SSIM of all the comparison methods on four benchmark datasets with the first simple synthesis setting. From it, we

Table 1: Average PSNR/SSIM of all the comparing methods (**Setting 1**).

Method	Scale	Urban100 [17]		BSD100 [28]		Set14 [52]		Set5 [4]	
		PSNR	SSIM	PSNR	SSIM	PSNR	SSIM	PSNR	SSIM
Bicubic	x2	24.23	0.7430	27.02	0.7472	27.13	0.7797	29.42	0.8666
RCAN [59]		24.69	0.7727	27.40	0.7710	27.54	0.8804	29.81	0.8797
IKC [14]		29.22	0.8752	30.51	0.8540	31.69	0.8789	34.31	0.9287
DASR [43]		30.63	0.9079	31.76	0.8901	32.93	0.9029	37.22	0.9515
DAN [25]		31.31	0.9165	31.93	0.8906	33.31	0.9085	37.54	0.9546
KXNet(ours)		31.48	0.9192	32.03	0.8941	33.36	0.9091	37.58	0.9552
Bicubic	x3	22.07	0.6216	24.93	0.6360	24.58	0.6671	26.19	0.7716
RCAN [59]		22.18	0.6366	25.06	0.6501	24.73	0.6800	26.37	0.7840
IKC [14]		26.85	0.8087	28.29	0.7724	29.41	0.8106	32.90	0.8997
DASR [43]		27.28	0.8307	28.85	0.7932	29.94	0.8266	33.78	0.9200
DAN [25]		27.94	0.8450	29.04	0.8001	30.24	0.8350	34.18	0.9237
KXNet(ours)		28.00	0.8457	29.06	0.8010	30.27	0.8340	34.22	0.9238
Bicubic	x4	20.96	0.5544	23.84	0.5780	23.25	0.6036	24.43	0.7045
RCAN [59]		20.96	0.5608	23.89	0.5865	23.30	0.6109	24.52	0.7148
IKC [14]		24.42	0.7112	26.55	0.6867	26.88	0.7301	29.83	0.8375
DASR [43]		25.49	0.7621	27.40	0.7238	28.26	0.7668	31.68	0.8854
DAN [25]		25.95	0.7787	27.53	0.7311	28.55	0.7749	31.96	0.8898
KXNet(ours)		26.18	0.7873	27.59	0.7330	28.67	0.7782	31.94	0.8912

Fig. 4: Performance comparison on *img 14* in Set14 [52] and *img 078* in Urban100 [17]. The scale factor is 4 and noise level is 5.

can easily find that the proposed KXNet is superior or at least comparable to other comparison methods under different scales. This is mainly attributed to its proper and full embedding of physical generation mechanism which finely helps the KXNet to be trained in the right direction.

Tab. 2 provides the quantitative comparison where testing sets are synthesized under the second complicated setting. Clearly, even in this hard case, our proposed KXNet still achieves the most competing performance and consistently outperforms other comparison methods on the four benchmark datasets with different SR scales. This comprehensively substantiates the generality of the proposed method and its potential usefulness in real-world scenarios.

Fig. 4 visually displays the SR results on *img014* from Set14 and *img078* from Urban100 where the corresponding LR images are synthesized based on the second settings. As seen, almost all the blind comparison methods cannot finely reconstruct the image details. However, our KXNet achieves superior SR performance and the SR images contain more useful textures and sharper edges.

Table 2: Average PSNR/SSIM of all the comparing methods (**Setting 2**).

Method	Scale	Urban100 [17]		BSD100 [28]		Set14 [52]		Set5 [4]		Noise Level
		PSNR	SSIM	PSNR	SSIM	PSNR	SSIM	PSNR	SSIM	
Bicubic	x2	23.00	0.6656	25.85	0.6769	25.74	0.7085	27.68	0.8047	0
RCAN [59]		23.22	0.6791	26.03	0.6896	25.92	0.7217	27.85	0.8095	
IKC [14]		27.46	0.8401	29.85	0.8390	30.69	0.8614	33.99	0.9229	
DASR [43]		26.65	0.8106	28.84	0.7965	29.44	0.8224	32.50	0.8961	
DAN [25]		27.93	0.8497	30.09	0.8410	31.03	0.8647	34.40	0.9291	
KXNet(ours)		28.33	0.8627	30.21	0.8456	31.14	0.8672	34.59	0.9315	
Bicubic	x3	21.80	0.6084	24.68	0.6254	24.28	0.6546	25.78	0.7555	
RCAN [59]		21.38	0.6042	24.47	0.6299	24.07	0.6606	25.63	0.7572	
IKC [14]		25.36	0.7626	27.56	0.7475	28.19	0.7805	31.60	0.8853	
DASR [43]		25.20	0.7575	27.39	0.7379	27.96	0.7727	30.91	0.8723	
DAN [25]		25.82	0.7855	27.88	0.7603	28.69	0.7969	31.70	0.8940	
KXNet(ours)		26.37	0.8035	28.15	0.7672	29.04	0.8036	32.53	0.9034	
Bicubic	x4	20.88	0.5602	23.75	0.5827	23.17	0.6082	24.35	0.7086	
RCAN [59]		19.84	0.5307	23.10	0.5729	22.38	0.5967	23.72	0.6973	
IKC [14]		24.33	0.7241	26.49	0.6968	27.04	0.7398	29.60	0.8503	
DASR [43]		24.20	0.7150	26.43	0.6903	26.89	0.7306	29.53	0.8455	
DAN [25]		24.91	0.7491	26.92	0.7168	27.69	0.7600	30.53	0.8746	
KXNet(ours)		25.30	0.7647	27.08	0.7221	27.98	0.7659	30.99	0.8815	
Bicubic	x2	22.19	0.5159	24.44	0.5150	24.38	0.5497	25.72	0.6241	
RCAN [59]		21.28	0.3884	22.98	0.3822	22.96	0.4155	23.76	0.4706	
IKC [14]		24.69	0.7208	26.49	0.6828	26.93	0.7244	29.21	0.8260	
DASR [43]		24.84	0.7273	26.63	0.6841	27.22	0.7283	29.44	0.8322	
DAN [25]		25.32	0.7447	26.84	0.6932	27.56	0.7392	29.91	0.8430	
KXNet(ours)		25.45	0.7500	26.87	0.6959	27.59	0.7422	29.93	0.8449	
Bicubic	x3	21.18	0.4891	23.55	0.4961	23.28	0.5289	24.42	0.6119	
RCAN [59]		20.22	0.3693	22.20	0.3726	21.99	0.4053	22.85	0.4745	
IKC [14]		24.21	0.7019	25.93	0.6564	26.42	0.7018	28.61	0.8135	
DASR [43]		23.93	0.6890	25.82	0.6484	26.27	0.6940	28.27	0.8047	
DAN [25]		24.17	0.7013	25.93	0.6551	26.46	0.7014	28.52	0.8130	
KXNet(ours)		24.42	0.7135	25.99	0.6585	26.56	0.7063	28.64	0.8178	
Bicubic	x4	20.38	0.4690	22.83	0.4841	22.39	0.5120	23.33	0.5977	
RCAN [59]		19.23	0.3515	21.47	0.3686	21.05	0.3960	21.77	0.4689	
IKC [14]		23.35	0.6665	25.21	0.6238	25.58	0.6712	27.45	0.7867	
DASR [43]		23.26	0.6620	25.20	0.6223	25.55	0.6683	27.32	0.7842	
DAN [25]		23.48	0.6742	25.25	0.6283	25.72	0.6760	27.55	0.7938	
KXNet(ours)		23.67	0.6844	25.30	0.6296	25.78	0.6792	27.66	0.7977	

5.3 More Analysis and Verification

Number of Iterations for KXNet. To explore the effectiveness of KXNet, we investigate the effect of the number of iterations on the performance of KXNet. In Tab. 3, $S = 0$ means that the initialization $\mathbf{X}^{(0)}$ and $\mathbf{K}^{(0)}$ are directly used as the recovery result. Taking $S = 0$ as a baseline, we can clearly see that when $S = 5$, our method has been able to achieve a significant recovery performance which strongly validates the effectiveness of K-net and X-net. Beside, since larger stages would make gradient propagation more difficult, the case $S = 21$ has the same PSNR to the case $S = 19$. Thus, we set $S = 19$ for this work.

Non-Blind Super-Resolution. We provide ground truth (GT) kernel to verify the effectiveness of KXNet and other method on Set14 [52]. Providing blur kernel for KXNet and DAN, namely KXNet(GT kernel) and DAN(GT kernel), the PSNR of the results are 32.85 and 32.67, respectively. While the baseline KXNet with unknown blur kernel is 31.97. This means that when we provide X-net with an accurate blur kernel, the restoration accuracy can be further improved while illustrating the rationality and superiority of X-net for image restoration.

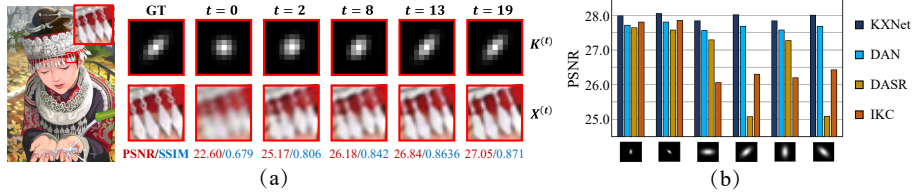


Fig. 5: (a) The estimated SR image and the extracted blur kernel at different iterative stages of KXNet. (b) Performance comparison under different blur kernel settings on Set14 [52] (scale = 4, noise = 0).

Table 3: Effect of stage number S on the performance of KXNet on Set14.

Stage No.	S=0	S=5	S=10	S=17	S=19	S=21
PSNR	25.74	29.91	30.57	30.96	31.14	31.14
SSIM	0.7085	0.8400	0.8556	0.8631	0.8672	0.8665
Params(M)	-	1.72	3.42	5.82	6.50	7.18
Speed(seconds)	-	0.51	0.54	0.58	0.59	0.64

Stage Visualization. Owing to the full embedding of the physical generation mechanism, the proposed KXNet can facilitate us to easily understand the iterative process via stage visualization. As shown in Fig. 5(a), it presents the estimated SR images and the predicted blur kernel at different stages, where the blur kernel is simply initialized as standard Gaussian kernel. Clearly, with the increasing of the iterative stages, the extracted blur kernel has a better and clearer pattern, which is getting closer to the GT kernel. Correspondingly, the SR image is gradually ameliorated and achieves higher PSNR/SSIM scores. This interpretable learning process is the inherent characteristic of the proposed KXNet which is finely guided by the mutual promotion between K-net and X-net.

Robustness to Blur Kernel. To comprehensively validate the effectiveness of the proposed method and its advantage over blur kernel extraction, we compare the SR performance of different methods on synthesized Set14 [52] with different blur kernel widths. As displayed in Fig. 5(b), as the structures of the testing blur kernels become more complex, the performance of most comparison methods has severely deteriorated. However, the proposed KXNet can consistently achieve the most competing PSNR scores and the fluctuation is very small. This result fully shows that our method has better robustness to the types of blur kernels and it has better potential to deal with general and real scenes.

5.4 Inference Speed

Based on Set5 under setting2 (scale=2, noise=0), we evaluate the inference time computed on an P100 GPU. For every image, the average testing time for IKC [14], DAN [25], and our proposed KXNet are shown in Tab. 4. Clearly, compared to these representative SOTA methods, our method has high inference speed and better computation efficiency, which is meaningful for real applications.

Table 4: Average inference speed of different methods on Set5.

Methods	IKC [14]	DAN [25]	KXNet
Times (s)	2.15	0.52	0.38

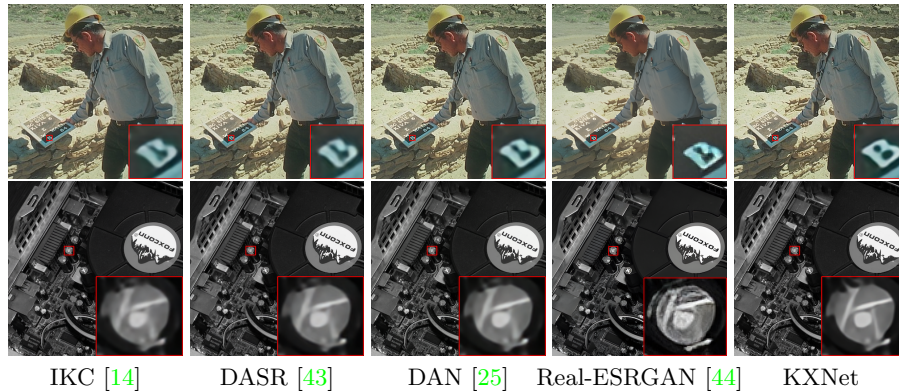


Fig. 6: Visual comparison on RealSRSet with scale factor as 4.

5.5 Experiments on Real Images

We further evaluate the effectiveness of our method for real-world image restoration on RealSRSet [54]. As shown in Fig. 6, the proposed KXNet can recover clearer edges and generate more useful information.

6 Conclusion

In this paper, we have proposed an end-to-end blind super-resolution network for SISR, named as KXNet. In specific, we analyze the classical degradation process of low-resolution (LR) images and utilize the proximal gradient technique to derive an optimization algorithm. By unfolding the iterative steps into network modules, we easily construct the entire framework which is composed of K-net and X-net, and the explicit physical generation mechanism of blur kernels and high-resolution (HR) images are fully incorporated into the entire learning process. Besides, the proposed KXNet has better potential to finely extract different types of blur kernels which should be useful for other related tasks. All these advantages have been fully substantiated by comprehensive experiments executed on synthesized and real-world data under different degradation settings. This also finely validates the effectiveness and generality of the proposed KXNet.

Acknowledgment. This research was supported by NSFC project under contracts U21A6005, 61721002, U1811461, 62076196, The Major Key Project of PCL under contract PCL2021A12, and the Macao Science and Technology Development Fund under Grant 061/2020/A2.

References

1. Agustsson, E., Timofte, R.: NTIRE 2017 challenge on single image super-resolution: Dataset and study. In: Proceedings of the IEEE Conference on Computer Vision and Pattern Recognition Workshops. pp. 126–135 (2017)
2. Beck, A., Teboulle, M.: A fast iterative shrinkage-thresholding algorithm for linear inverse problems. *SIAM Journal on Imaging Sciences* **2**(1), 183–202 (2009)
3. Bell-Kligler, S., Shocher, A., Irani, M.: Blind super-resolution kernel estimation using an internal-gan. *Advances in Neural Information Processing Systems* **32** (2019)
4. Bevilacqua, M., Roumy, A., Guillemot, C., Alberi-Morel, M.L.: Low-complexity single-image super-resolution based on nonnegative neighbor embedding. In: Proceedings of the British Machine Vision Conference. pp. 135.1–135.10. BMVA press (2012)
5. Brifman, A., Romano, Y., Elad, M.: Unified single-image and video super-resolution via denoising algorithms. *IEEE Transactions on Image Processing* **28**(12), 6063–6076 (2019)
6. Dai, S., Han, M., Xu, W., Wu, Y., Gong, Y., Katsaggelos, A.K.: SoftCuts: a soft edge smoothness prior for color image super-resolution. *IEEE Transactions on Image Processing* **18**(5), 969–981 (2009)
7. Dong, C., Loy, C.C., He, K., Tang, X.: Image super-resolution using deep convolutional networks. *IEEE Transactions on Pattern Analysis and Machine Intelligence* **38**(2), 295–307 (2015)
8. Donoho, D.L.: De-noising by soft-thresholding. *IEEE Transactions on Information Theory* **41**(3), 613–627 (1995)
9. Dumoulin, V., Visin, F.: A guide to convolution arithmetic for deep learning. arXiv preprint arXiv:1603.07285 (2016)
10. Efrat, N., Glasner, D., Apartsin, A., Nadler, B., Levin, A.: Accurate blur models vs. image priors in single image super-resolution. In: Proceedings of the IEEE International Conference on Computer Vision. pp. 2832–2839 (2013)
11. Elad, M., Feuer, A.: Restoration of a single superresolution image from several blurred, noisy, and undersampled measured images. *IEEE Transactions on Image Processing* **6**(12), 1646–1658 (1997)
12. Farsiu, S., Robinson, D., Elad, M., Milanfar, P.: Advances and challenges in super-resolution. *International Journal of Imaging Systems and Technology* **14**(2), 47–57 (2004)
13. Gregor, K., LeCun, Y.: Learning fast approximations of sparse coding. In: Proceedings of the 27th International Conference on International Conference on Machine Learning. pp. 399–406 (2010)
14. Gu, J., Lu, H., Zuo, W., Dong, C.: Blind super-resolution with iterative kernel correction. In: Proceedings of the IEEE/CVF Conference on Computer Vision and Pattern Recognition. pp. 1604–1613 (2019)
15. He, K., Zhang, X., Ren, S., Sun, J.: Deep residual learning for image recognition. In: Proceedings of the IEEE Conference on Computer Vision and Pattern Recognition. pp. 770–778 (2016)
16. Heide, F., Diamond, S., Nießner, M., Ragan-Kelley, J., Heidrich, W., Wetzstein, G.: Proximal: Efficient image optimization using proximal algorithms. *ACM Transactions on Graphics (TOG)* **35**(4), 1–15 (2016)
17. Huang, J.B., Singh, A., Ahuja, N.: Single image super-resolution from transformed self-exemplars. In: Proceedings of the IEEE Conference on Computer Vision and Pattern Recognition. pp. 5197–5206 (2015)

18. Ignatov, A., Kobyshev, N., Timofte, R., Vanhoey, K., Van Gool, L.: DSLR-quality photos on mobile devices with deep convolutional networks. In: Proceedings of the IEEE International Conference on Computer Vision. pp. 3277–3285 (2017)
19. Kim, J., Lee, J.K., Lee, K.M.: Deeply-recursive convolutional network for image super-resolution. In: Proceedings of the IEEE Conference on Computer Vision and Pattern Recognition. pp. 1637–1645 (2016)
20. Kingma, D.P., Ba, J.: ADAM: A method for stochastic optimization. arXiv preprint arXiv:1412.6980 (2014)
21. Lai, W.S., Huang, J.B., Ahuja, N., Yang, M.H.: Deep laplacian pyramid networks for fast and accurate super-resolution. In: Proceedings of the IEEE Conference on Computer Vision and Pattern Recognition. pp. 624–632 (2017)
22. Liang, J., Cao, J., Sun, G., Zhang, K., Van Gool, L., Timofte, R.: SwinIR: Image restoration using swin transformer. In: Proceedings of the IEEE/CVF International Conference on Computer Vision. pp. 1833–1844 (2021)
23. Liang, J., Zhang, K., Gu, S., Van Gool, L., Timofte, R.: Flow-based kernel prior with application to blind super-resolution. In: Proceedings of the IEEE/CVF Conference on Computer Vision and Pattern Recognition. pp. 10601–10610 (2021)
24. Lim, B., Son, S., Kim, H., Nah, S., Mu Lee, K.: Enhanced deep residual networks for single image super-resolution. In: Proceedings of the IEEE Conference on Computer Vision and Pattern Recognition Workshops. pp. 136–144 (2017)
25. Luo, Z., Huang, Y., Li, S., Wang, L., Tan, T.: Unfolding the alternating optimization for blind super resolution. *Advances in Neural Information Processing Systems (NeurIPS)* **33** (2020)
26. Luo, Z., Huang, Y., Li, S., Wang, L., Tan, T.: End-to-end alternating optimization for blind super resolution. arXiv preprint arXiv:2105.06878 (2021)
27. Marquina, A., Osher, S.J.: Image super-resolution by TV-regularization and bregman iteration. *Journal of Scientific Computing* **37**(3), 367–382 (2008)
28. Martin, D., Fowlkes, C., Tal, D., Malik, J.: A database of human segmented natural images and its application to evaluating segmentation algorithms and measuring ecological statistics. In: Proceedings Eighth IEEE International Conference on Computer Vision. ICCV 2001. vol. 2, pp. 416–423. IEEE (2001)
29. Matsui, Y., Ito, K., Aramaki, Y., Fujimoto, A., Ogawa, T., Yamasaki, T., Aizawa, K.: Sketch-based manga retrieval using manga109 dataset. *Multimedia Tools and Applications* **76**(20), 21811–21838 (2017)
30. Michaeli, T., Irani, M.: Nonparametric blind super-resolution. In: Proceedings of the IEEE International Conference on Computer Vision. pp. 945–952 (2013)
31. Niu, B., Wen, W., Ren, W., Zhang, X., Yang, L., Wang, S., Zhang, K., Cao, X., Shen, H.: Single image super-resolution via a holistic attention network. In: European Conference on Computer Vision. pp. 191–207. Springer (2020)
32. Pan, J., Sun, D., Pfister, H., Yang, M.H.: Blind image deblurring using dark channel prior. In: Proceedings of the IEEE Conference on Computer Vision and Pattern Recognition. pp. 1628–1636 (2016)
33. Perrone, D., Favaro, P.: Total variation blind deconvolution: The devil is in the details. In: Proceedings of the IEEE Conference on Computer Vision and Pattern Recognition. pp. 2909–2916 (2014)
34. Ren, D., Zhang, K., Wang, Q., Hu, Q., Zuo, W.: Neural blind deconvolution using deep priors. In: Proceedings of the IEEE/CVF Conference on Computer Vision and Pattern Recognition. pp. 3341–3350 (2020)
35. Riegler, G., Schuler, S., Ruther, M., Bischof, H.: Conditioned regression models for non-blind single image super-resolution. In: Proceedings of the IEEE International Conference on Computer Vision. pp. 522–530 (2015)

36. Shi, W., Caballero, J., Theis, L., Huszar, F., Aitken, A., Ledig, C., Wang, Z.: Is the deconvolution layer the same as a convolutional layer? arXiv preprint arXiv:1609.07009 (2016)
37. Sun, L., Cho, S., Wang, J., Hays, J.: Edge-based blur kernel estimation using patch priors. In: IEEE International Conference on Computational Photography (ICCP). pp. 1–8. IEEE (2013)
38. Timofte, R., Agustsson, E., Van Gool, L., Yang, M.H., Zhang, L.: NTIRE 2017 challenge on single image super-resolution: Methods and results. In: Proceedings of the IEEE Conference on Computer Vision and Pattern Recognition Workshops. pp. 114–125 (2017)
39. Wang, H., Li, Y., He, N., Ma, K., Meng, D., Zheng, Y.: DICDNet: Deep interpretable convolutional dictionary network for metal artifact reduction in CT images. IEEE Transactions on Medical Imaging **41**(4), 869–880 (2021)
40. Wang, H., Li, Y., Zhang, H., Chen, J., Ma, K., Meng, D., Zheng, Y.: InDuDoNet: An interpretable dual domain network for CT metal artifact reduction. In: International Conference on Medical Image Computing and Computer-Assisted Intervention. pp. 107–118. Springer (2021)
41. Wang, H., Xie, Q., Zhao, Q., Liang, Y., Meng, D.: RCDNet: An interpretable rain convolutional dictionary network for single image deraining. arXiv preprint arXiv:2107.06808 (2021)
42. Wang, H., Xie, Q., Zhao, Q., Meng, D.: A model-driven deep neural network for single image rain removal. In: Proceedings of the IEEE/CVF Conference on Computer Vision and Pattern Recognition. pp. 3103–3112 (2020)
43. Wang, L., Wang, Y., Dong, X., Xu, Q., Yang, J., An, W., Guo, Y.: Unsupervised degradation representation learning for blind super-resolution. In: Proceedings of the IEEE/CVF Conference on Computer Vision and Pattern Recognition. pp. 10581–10590 (2021)
44. Wang, X., Xie, L., Dong, C., Shan, Y.: Real-ESRGAN: Training real-world blind super-resolution with pure synthetic data. In: Proceedings of the IEEE/CVF International Conference on Computer Vision. pp. 1905–1914 (2021)
45. Wang, Z., Bovik, A.C., Sheikh, H.R., Simoncelli, E.P.: Image quality assessment: from error visibility to structural similarity. IEEE Transactions on Image Processing **13**(4), 600–612 (2004)
46. Xie, Q., Zhou, M., Zhao, Q., Meng, D., Zuo, W., Xu, Z.: Multispectral and hyperspectral image fusion by MS/HS fusion net. In: Proceedings of the IEEE/CVF Conference on Computer Vision and Pattern Recognition. pp. 1585–1594 (2019)
47. Xie, Q., Zhou, M., Zhao, Q., Xu, Z., Meng, D.: MHF-Net: An interpretable deep network for multispectral and hyperspectral image fusion. IEEE Transactions on Pattern Analysis and Machine Intelligence (2020)
48. Xu, Y.S., Tseng, S.Y.R., Tseng, Y., Kuo, H.K., Tsai, Y.M.: Unified dynamic convolutional network for super-resolution with variational degradations. In: Proceedings of the IEEE/CVF Conference on Computer Vision and Pattern Recognition. pp. 12496–12505 (2020)
49. Yan, Y., Ren, W., Guo, Y., Wang, R., Cao, X.: Image deblurring via extreme channels prior. In: Proceedings of the IEEE Conference on Computer Vision and Pattern Recognition. pp. 4003–4011 (2017)
50. Yang, D., Sun, J.: Proximal Dehaze-Net: A prior learning-based deep network for single image dehazing. In: Proceedings of the European Conference on Computer Vision (ECCV). pp. 702–717 (2018)

51. Yang, Y., Sun, J., Li, H., Xu, Z.: Deep ADMM-Net for compressive sensing MRI. In: Proceedings of the 30th International Conference on Neural Information Processing Systems. pp. 10–18 (2016)
52. Zeyde, R., Elad, M., Protter, M.: On single image scale-up using sparse-representations. In: International Conference on Curves and Surfaces. pp. 711–730. Springer (2010)
53. Zhang, K., Gool, L.V., Timofte, R.: Deep unfolding network for image super-resolution. In: Proceedings of the IEEE/CVF Conference on Computer Vision and Pattern Recognition. pp. 3217–3226 (2020)
54. Zhang, K., Liang, J., Van Gool, L., Timofte, R.: Designing a practical degradation model for deep blind image super-resolution. In: Proceedings of the IEEE/CVF International Conference on Computer Vision. pp. 4791–4800 (2021)
55. Zhang, K., Zuo, W., Gu, S., Zhang, L.: Learning deep CNN denoiser prior for image restoration. In: Proceedings of the IEEE Conference on Computer Vision and Pattern Recognition. pp. 3929–3938 (2017)
56. Zhang, K., Zuo, W., Zhang, L.: FFDNet: Toward a fast and flexible solution for CNN-based image denoising. *IEEE Transactions on Image Processing* **27**(9), 4608–4622 (2018)
57. Zhang, K., Zuo, W., Zhang, L.: Learning a single convolutional super-resolution network for multiple degradations. In: Proceedings of the IEEE Conference on Computer Vision and Pattern Recognition. pp. 3262–3271 (2018)
58. Zhang, K., Zuo, W., Zhang, L.: Deep plug-and-play super-resolution for arbitrary blur kernels. In: Proceedings of the IEEE/CVF Conference on Computer Vision and Pattern Recognition. pp. 1671–1681 (2019)
59. Zhang, Y., Li, K., Li, K., Wang, L., Zhong, B., Fu, Y.: Image super-resolution using very deep residual channel attention networks. In: Proceedings of the European Conference on Computer Vision (ECCV). pp. 286–301 (2018)
60. Zhang, Y., Tian, Y., Kong, Y., Zhong, B., Fu, Y.: Residual dense network for image super-resolution. In: Proceedings of the IEEE Conference on Computer Vision and Pattern Recognition. pp. 2472–2481 (2018)
61. Zhao, H., Gallo, O., Frosio, I., Kautz, J.: Loss functions for image restoration with neural networks. *IEEE Transactions on Computational Imaging* **3**(1), 47–57 (2016)